Article

$S_2O_8^{2-}$/CeO$_2$ Solid Superacid Catalyst Prepared by Radio-Frequency Plasma-Assisted Hydrothermal Method

Kaiqiang Wang [1,†], **Changhui Zhu** [1,†], **Xudong Zhang** [2], **Baohe Tian** [1], **Wenchao Zhu** [1,*] and **Bangdou Huang** [3,*]

1 State Key Laboratory of NBC Protection for Civilian, Beijing 102205, China; wangkaiqiang2647@163.com (K.W.); zhuchanghui567@163.com (C.Z.); tbh318@sohu.com (B.T.)
2 School of Mechanical Engineering, Sichuan University of Science and Engineering, Yibin 644000, China; onlyfaith44@163.com
3 Beijing International S&T Cooperation Base for Plasma Science and Energy Transformation, Institute of Electrical Engineering, Chinese Academy of Sciences, Beijing 100190, China
* Correspondence: zhuwenchao_2007@tsinghua.org.cn (W.Z.); huangbangdou@mail.iee.ac.cn (B.H.)
† These authors contributed equally to this work.

Abstract: CeO$_2$ was prepared using a hydrothermal method, modified by radio-frequency plasma in the form of glow discharge, and then the solid superacid $S_2O_8^{2-}$/CeO$_2$ was prepared by the impregnation method. A series of properties such as pore structure was characterized by N$_2$ adsorption–desorption experiments, surface morphology was characterized by TEM, crystal phase was characterized by XRD, and surface acidity of the catalyst was characterized by Py-IR and Hammett titration. The methyl esterification reaction of tryptophan was used to evaluate the activity of the solid superacid. The results showed that the catalyst modified by radio-frequency plasma had a larger specific surface area, more surface oxygen vacancies, smaller particle size, and higher total acid content. The yield of tryptophan methyl ester reached a higher level of 94.5% (150 °C, 1 MPa, 2 h), catalyzed by the modified $S_2O_8^{2-}$/CeO$_2$. This work verified the feasibility of plasma technology in the field of catalytic activity enhancement of solid superacid.

Keywords: CeO$_2$; radio-frequency plasma; solid superacid $S_2O_8^{2-}$/CeO$_2$; esterification of tryptophan

1. Introduction

Solid superacid refers to an acid that is stronger than 100% H$_2$SO$_4$ with a Hammett function $H_0 < -11.93$ [1]. Since Hino discovered the SO_4^{2-}/M$_x$O$_y$-type solid superacid catalyst and applied it to the isomerization reaction of *n*-butane [2], many researchers have investigated modified SO_4^{2-}/M$_x$O$_y$, using it in diverse reactions. SO_4^{2-}/M$_x$O$_y$ is composed of active component SO_4^{2-} and carrier M$_x$O$_y$. Wherein SO_4^{2-} can usually be replaced by $S_2O_8^{2-}$ [3], as $S_2O_8^{2-}$ has a higher sulfur content under the same molar mass, which is beneficial in improving catalyst activity, moreover, $S_2O_8^{2-}$ has stronger electron-withdrawing capacity [4]. The modification of the carrier usually includes the introduction of metals [5] (rare-earth elements [6]), metal oxides [7–9], molecular sieves [10] and so on. However, the introduction of other components into the carrier will not only complicate the preparation process but also increase the cost. Therefore, it has positive significance to prepare $S_2O_8^{2-}$/M$_x$O$_y$ catalysts using specific modification technology without introducing other elements.

Plasma is an ionized gas composed of electrons, ions, and neutral particles, whose overall state is approximately electrically neutral [11], with positive and negative ions produced by the ionization of atoms and atomic clusters [12]. According to the temperature of plasma gas, it can be divided into low-temperature plasma (<10^3 K) and high-temperature plasma (>10^9 K) [13]. Wherein the gas in low-temperature plasma is only partially ionized, which contains thermal equilibrium plasma and non-thermal equilibrium plasma as well. In non-thermal equilibrium plasma, the electron temperature can be as high as

10^3 K, but the temperature of heavy particles (ions, atoms, etc.) is only 300 K, which is close to room temperature, mainly including glow discharge, corona discharge, dielectric barrier discharge, etc. [14]. The power drive mode mainly warrants high-frequency pulse, radio frequency, microwave, etc. An electric field on the surface of materials can be formed by low-temperature plasma, due to its smaller electron mass and faster velocity, causing mutual repulsion and improving the dispersion of particles [15]. Consequently, low-temperature plasma can be applied to catalyst modification. To illustrate this, Wang et al. prepared and modified CeO_2 nanorod-loaded Ni catalysts by glow discharge plasma, and the results showed this treatment can enhance the dispersion of Ni, improving the interaction of Ni–Ce bonds and inhibiting the formation of carbon deposition in the reaction process. [16] Li and fellows modified the Pd precursor with non-thermal radio frequency (RF) plasma. The results showed that the precursor modified by RF plasma not only was effectively reduced to Pd^0, but also improved the dispersion of Pd^0 particles [17].

The above research mainly used plasma to enhance chemical bond interactions between metal oxide in the precursor, but there are few studies on the preparation of $S_2O_8^{2-}/M_xO_y$ solid superacid by modifying the carrier M_xO_y with plasma treatment. As low-temperature plasma also has the function of etching and creating vacancies, increasing the number of active sites on the materials surface. For instance, Xu and colleagues [18] used Ar RF plasma to treat Co_3O_4 nano-sheets, which can not only create etching phenomenon on nano-sheets, but also produce oxygen vacancies, thus deducing RF plasma can assist in the preparation of CeO_2 with more oxygen vacancies [19]. Hence, RF plasma has the application potential for the modification of carrier CeO_2, applying for the preparation of solid superacid to some extent.

In recent years, α-Aromatic amino acid esters (AAAE) and their derivatives have been widely used in intermediates of drug synthesis, food additives, and other industries [20–22]. Tryptophan methyl ester (TrpOMe, the methyl esterification reaction of tryptophan is shown in Figure 1), as one compound of the AAAE, is a key platform compound for the synthesis of sweeteners and the manufacturing of fluorescent sensors [23]. However, owing to amphoteric dissociations, leading to the esterification reaction of tryptophan (Trp) difficulties under mild conditions, therefore, its reaction equilibrium needs to be achieved with the assistance of strong acid catalysts.
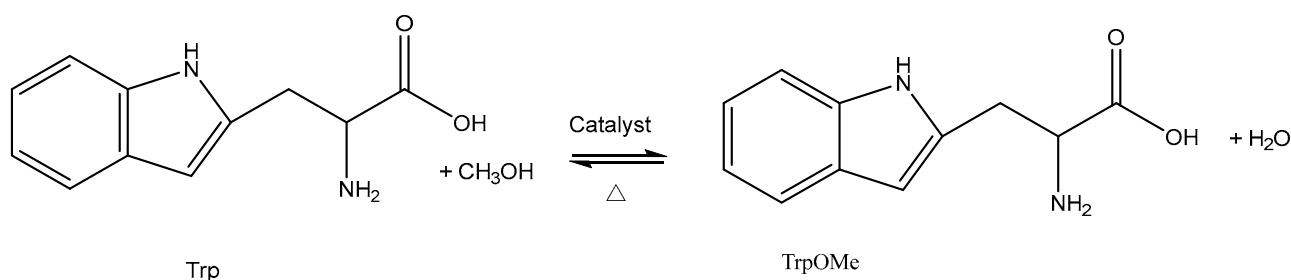
Figure 1. The methyl esterification reaction of Trp.

Based on the above background, nano-CeO_2 was prepared using the hydrothermal method. After the modification of RF plasma, $S_2O_8^{2-}$ was loaded onto nano-CeO_2 and then calcined (at 600 °C) to manufacture $S_2O_8^{2-}/CeO_2$-RF-600 (SC-RF-600) solid superacid, which was used for the esterification of Trp. Finally, the properties of SC-RF-600, such as pore structure, surface morphology, crystal phase, and surface acidity, were evaluated and showed that RF plasma technology had a positive effect on the esterification ability of SC-RF-600 over Trp, thus facilitating a successful application of plasma technology in enhancing the catalytic activity of a solid superacid.

2. Results and Discussion

2.1. Hammett Titration

In the Hammett titration experiment of SC-RF-600, the results and color change of the catalyst surface are illustrated in Table 1 and Figure 2, respectively. The plus sign (+) indicated that the acid strength of the solid superacid was higher than that of the indicator. From the titration experiment, it was confirmed that the H_0 range of SC-RF-600 was $H_0 \leq -14.5$, as the H_0 of concentrated H_2SO_4 is ~10.44 [24]. SC-RF-600 therefore was a solid superacid.

Table 1. Acid strengths of SC-RF-600 using the titration of a different Hammett indicator.

Indicator	2,4-DNFB	3-NT
H_0	≤ -14.5	≤ -12.0
Result	+	+

Note: +, The color of the catalyst surface changed from light gray to yellow.
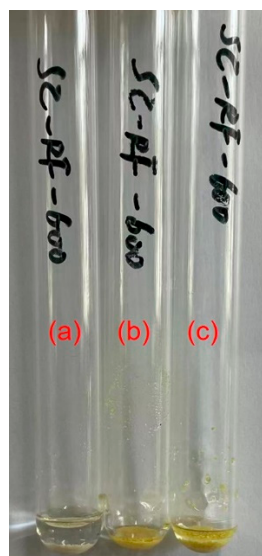
Figure 2. Hammett titration of SC-RF-600: (**a**) before titration, (**b**) after 3-NT titration, (**c**) after 2,4-DNFB titration.

2.2. XRD

The XRD spectra of these samples are shown in Figure 3. The diffraction peaks at *2θ* of 28.5°, 33.1°, 47.5°, 56.3°, 59.1°, 69.4°, 76.7°, 79.1°, and 88.4° were assigned to corresponding (111), (200), (220), (311), (222), (400), (331), (420), and (422) crystal planes of CeO$_2$, consistent with JCPDS card No. 043-1002. It is widely acknowledged that intact crystal forms are one of the necessary conditions for the formation of a superacid [25]. As the temperature increased, the characteristic diffraction peaks of CeO$_2$ were thereby enhanced, and the crystal form tended to be regular, showing a face-centered cubic fluorite structure. Compared with SC-600, the full width at half maximum (FWHM) of SC-RF-600 was larger. According to the Scherrer equation (Equation (1)) [26], the larger value of FWHM of SC-RF-600, the smaller the particle size of SC-RF-600.

$$D_\mathrm{C} = \frac{0.89\lambda}{B\cos\theta} \tag{1}$$

where, *B* was FWHM; λ referred to X-ray wavelength; θ was the diffraction angle.
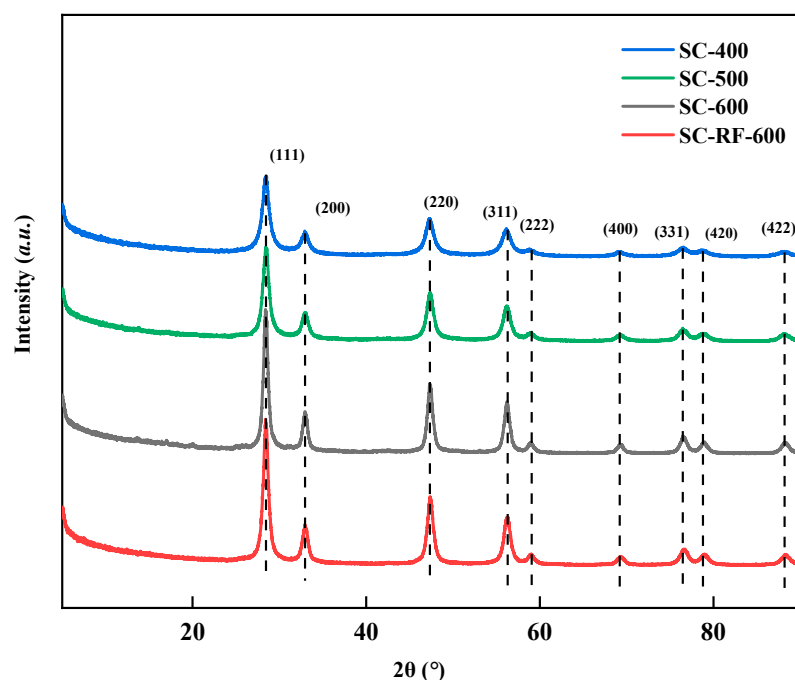
Figure 3. XRD patterns of the catalysts.

The average particle size of SC-400, SC-500, SC-600, and SC-RF-600 was 11.6 nm, 12.1 nm, 14.2 nm, and 12.6 nm, respectively, as calculated by Jade 6 6. 5. 26 (Materials Data Inc., Livermore, CA, USA) using Equation (1) based on others' work [27,28]. With the increase in temperature, grain size and crystallinity were increased. When compared with the unmodified catalyst, the grain size of the catalyst modified by RF plasma was smaller. This showed that CeO_2 modified by RF plasma effectively inhibited grain growth. This may be related to the fact that electrons were gathered around CeO_2 after RF plasma treatment, which made particles mutually repel, thus improving the dispersion of particles [15].

2.3. HR-TEM

The two type catalysts were tested by HR-TEM, and microscopic morphology images are shown in Figure 4, with the particle size distribution of SC-400, SC-500, SC-600, and SC-RF-600 shown in Figure 4a,c,e,g, respectively. It was observed that CeO_2 was mainly distributed in the form of rods, with average transverse diameters (~50 particles were measured) of 10.05 nm, 11.33 nm, 12.33 nm, and 10.36 nm, respectively, which generated the same trend and was consistent with XRD result (11.6 nm, 12.1 nm, 14.2 nm, and 12.6 nm, respectively). The longitudinal length was uneven, which was in the range of 27.7–143.6 nm, 22.5–223.5 nm, 28.9–142.3 nm, and 40.9–269.8 nm, respectively. Undoubtedly, the surface of CeO_2 nanorods modified by RF plasma possessed a larger number of pits compared with the other three samples, which was caused by the etching effects of high-energy particles in RF plasma, continuously bombarding the CeO_2 surface. Therefore, the specific surface area of CeO_2 was increased, and caused the dislocation of CeO_2 lattice defects and oxygen vacancies. A shown, Figure 4b,d,f,h corresponded to the HR-TEM images of the four catalysts. Combined with the analysis of Fast Fourier transform (FFT), three lattice fringes of (111), (200), and (220) were clearly observed, with lattice spacings of 0.31 nm, 0.27 nm, and 0.19 nm, respectively [29]. Wherein CeO_2 nanorods mainly exposed the (110) and (100) planes, showed a one-dimensional growth structure with preferential growth along the (110) crystal direction, and provided CeO_2 nanorods with a higher lattice oxygen mobility [30].
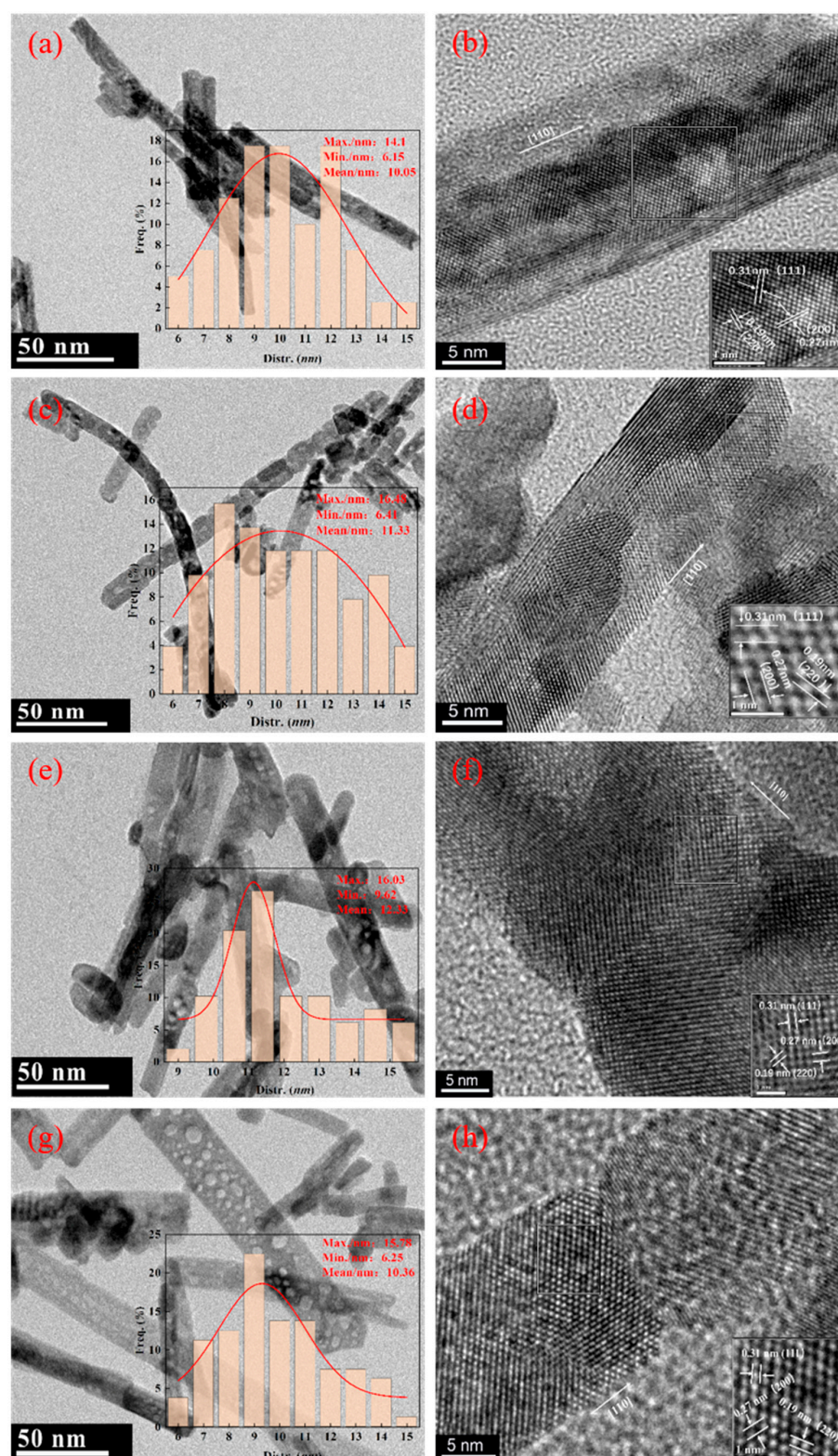
Figure 4. TEM images showing the particle size distribution of (**a**) SC-400, (**c**) SC-500, (**e**) SC-600 (**g**) SC-RF-600. HR-TEM images showing FFT analysis of (**b**) SC-400, (**d**) SC-500, (**f**) SC-600, (**h**) SC-RF-600.

2.4. FT-IR

The FT-IR spectra of the catalysts are shown in Figure 5. At 1627 cm^{-1}, we observed the bending vibration peak of physically adsorbed water on the sample surface [31]. The

band at 900–1300 cm^{-1} corresponded to O=S=O and O-S-O anti-symmetric stretching vibration and symmetric stretching vibration peak. The broad bands at 1030–1080 cm^{-1}, 1120–1150 cm^{-1}, and 1396 cm^{-1} are indexed to the characteristic peaks of $S_2O_8^{2-}/M_xO_y$ solid superacid [10,32]. The absorption peak at 985 cm^{-1} is related to the symmetrical tensile vibration of S-O, which is the characteristic peak of sulfate metal oxide [5,33]. The broad bands at 1280 cm^{-1} and 1164 cm^{-1} correspond to the antisymmetric O=S=O tensile vibration on persulfate ions. From the above analysis, the characteristic vibrational peaks of S=O and S-O bonds confirmed the existence of a superacid structure in the four samples [34]. In $S_2O_8^{2-}/M_xO_y$, the coordination form is distinguished according to the position corresponding to the infrared absorption of S=O stretching vibration. The metal ions of M_xO_y and $S_2O_8^{2-}$ were combined in the form of bridging bi-coordination with an absorption peak above 1200 cm^{-1} or chelate bi-coordination with an absorption peak below 1200 cm^{-1} [35]. The three catalysts had absorption peaks above 1200 cm^{-1} and below 1200 cm^{-1} in Figure 5b–d, except for SC-400 in Figure 5a, demonstrating the acid center structure was formed with the coordination of bridging bi-coordination and chelate bi-coordination. In comparison, SC-RF-600 in Figure 5d had stronger absorption peaks at 1396 cm^{-1}, 1280 cm^{-1}, 1120 cm^{-1}, and 1048 cm^{-1}. This may be caused by the increase in oxygen vacancies after RF modification, hence forming more coordination bonds.
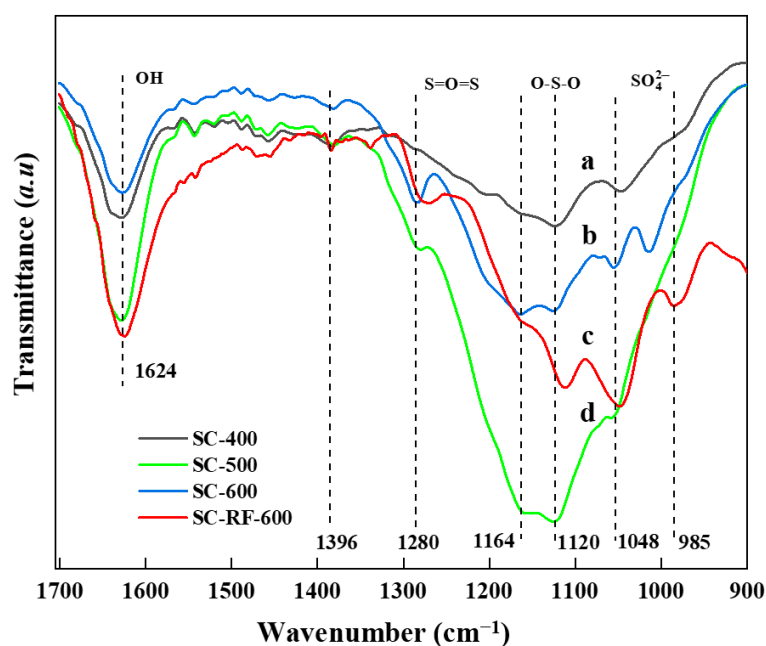

Figure 5. FT-IR spectra of the catalysts: (**a**) SC-400, (**b**) SC-600, (**c**) SC-RF-600, (**d**) SC-500.

2.5. Py-IR

Py-IR analysis was carried out to evaluate the surface acid density, and the results are shown in Figure 6. It was found that the trend of acid distributions was consistent at 150 °C and 300 °C (Figure S1 and Table S1), hence, we just adopted the test result at 150 °C close to the experimental environment. The bands at about 1550 cm^{-1} and 1630 cm^{-1} represent Brönsted acid (BA) sites; the bands at about 1440 cm^{-1} and 1600 cm^{-1} belong to Lewis acid (LA) sites; and the band at around 1490 cm^{-1} corresponds to BA sites and/or LA sites [36]. The acid density of each catalyst is shown in Table 2: as the temperature increased, the density of BA was increased, while the density of LA and total acid were increased firstly and then decreased (Entrys 1–3). This may be due to an increase in particle size, reduction of specific surface area and oxygen vacancies caused by calcination at the higher temperature (see Sections 2.2 and 2.3 for detailed analysis), thereby resulting in a decrease in LA sites, thus reducing LA sites. The BA density/LA density value of SC-RF-600 was low, but the BA density, LA density, and total acid density were the

largest (Entry 4). Additionally, the BA and LA density of SC-600 was 14.52 $\mu mol \cdot g^{-1}$ and 30.80 $\mu mol \cdot g^{-1}$ (Entry 3), respectively. However, the BA density of SC-RF-600 modified by RF plasma remained basically unchanged at 13.83 $\mu mol \cdot g^{-1}$, and the LA density was increased and almost doubled to 65.66 $\mu mol \cdot g^{-1}$ (Entry 4). From the above analysis, RF had a significant effect on the LA density of the solid superacid.
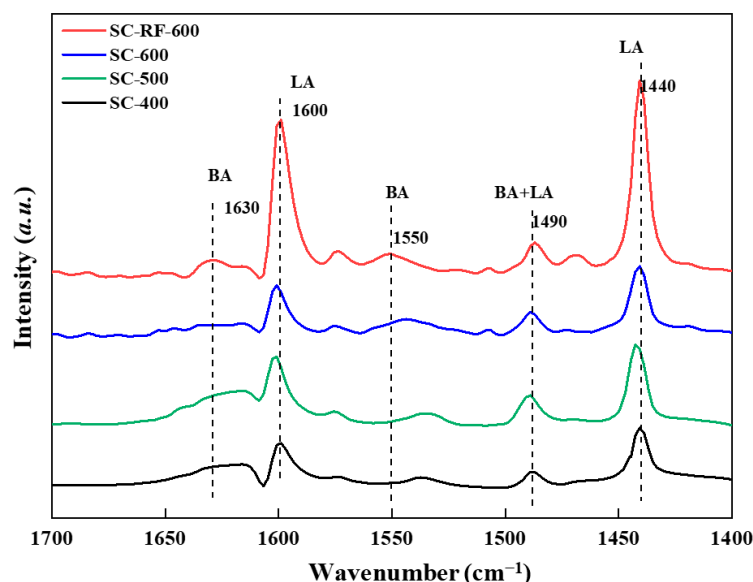

**Figure 6.** Py-IR spectra of the catalysts.

Table 2. Summary of acid density of the catalysts.

Entry	Cat.	BA Density ($\mu mol \cdot g^{-1}$)	LA Density ($\mu mol \cdot g^{-1}$)	Total Acid Density ($\mu mol \cdot g^{-1}$)	BA Density/LA Density
1	SC-400	7.33	36.56	43.89	0.20
2	SC-500	9.81	38.84	48.65	0.25
3	SC-600	14.52	30.80	45.32	0.47
4	SC-RF-600	13.83	65.66	79.49	0.21

2.6. N_2 Adsorption–Desorption Experiments

The N_2 adsorption–desorption isotherms of the samples tested twice are depicted in Figure 7. In Figure 7a,b, according to the classification of the IUPAC, these samples presented atypical type IV isotherms, along with the hysteresis loop isotherm which had no obvious saturated adsorption platform and belonged to the H3 type [5], indicating that the stacking of nanorods led to irregular pore structures. The pore size distributions of the catalyst are displayed in Figure 7c,d; the average pore size of SC-RF-600 was ~36.01 nm and was ascribed to mesoporous structure. The pore structure properties of the catalyst are illustrated in Table 3. As the temperature increased, the pore volume increased (Entrys 1–3). As the crystallinity of SC-400 and SC-500 was low, and they possessed more amorphous CeO_2 when calcined at 400 °C and 500 °C, hence the specific surface area was increased accordingly (Entrys 1 and 2). However, part of the micropores over CeO_2 collapsed into large pores at 600 °C, as a higher temperature can cause grain growth and reduce the specific surface area [37]. Noticeably, SC-RF-600 had the largest specific surface area (37.60 m^2/g, Entry 4), the pore volume of SC-RF-600 (0.33 cm^3/g, Entry 4) was larger, but the pore size was smaller (36.01 nm, Entry 4) when compared with those of SC-600 (36.08 nm, Entry 3). In summary, RF modification could effectively avoid the agglomeration of CeO_2 caused by high temperatures, improving the dispersion of CeO_2 and increasing the specific surface area accordingly.
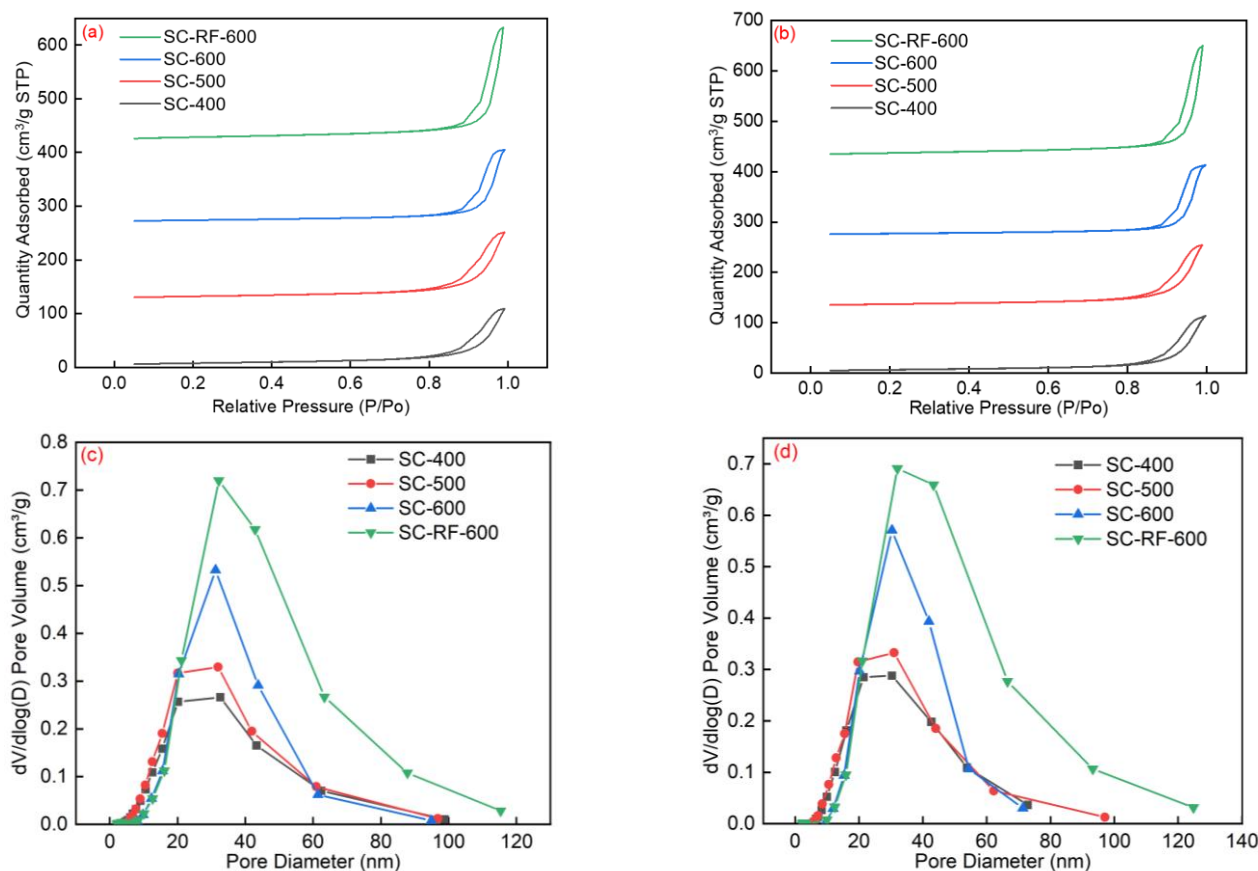
Figure 7. (**a**,**b**) N$_2$ adsorption–desorption isotherms and (**c**,**d**) the corresponding pore size distribution of catalysts.

Table 3. Structural parameters of the catalysts.

Entry	Sample	S$_{BET}$ Average Value (m^2/g)	S$_{BET}$ Standard Error (%)	Pore Volume Average Value (cm^3/g)	Pore Volume Standard Error (%)	Pore Size Average Value (nm)	Pore Size Standard Error (%)
1	SC-400	25.61	2.81	0.16	0.01	25.82	2.99
2	SC-500	28.87	1.41	0.19	0	26.77	1.40
3	SC-600	23.46	2.23	0.21	0	36.08	3.81
4	SC-RF-600	37.60	1.31	0.33	0.01	36.01	2.00

2.7. XPS

To further characterize the chemical composition of the catalyst surface, Ce, S, O and C elements in sample were analyzed by XPS, as shown in Figure 8. In Figure 8a, the Ce 3d can be deconvoluted into 10 Ce 3d peaks generated from the pairs of spin–orbit doublets. The six peaks at 882.4 eV, 888.7 eV, 898.67 eV, 900.1 eV, 907.7 eV, and 916.6 eV were assigned to Ce^{4+}, and the four peaks at 880.2 eV, 884.6 eV, 897.6 eV, and 902.6 eV were indexed to Ce^{3+}. The results showed that Ce in the catalyst mainly existed with +4 valence [Ce^{3+}/(Ce^{3+} + Ce^{4+}) = 31.36%] [19,38].
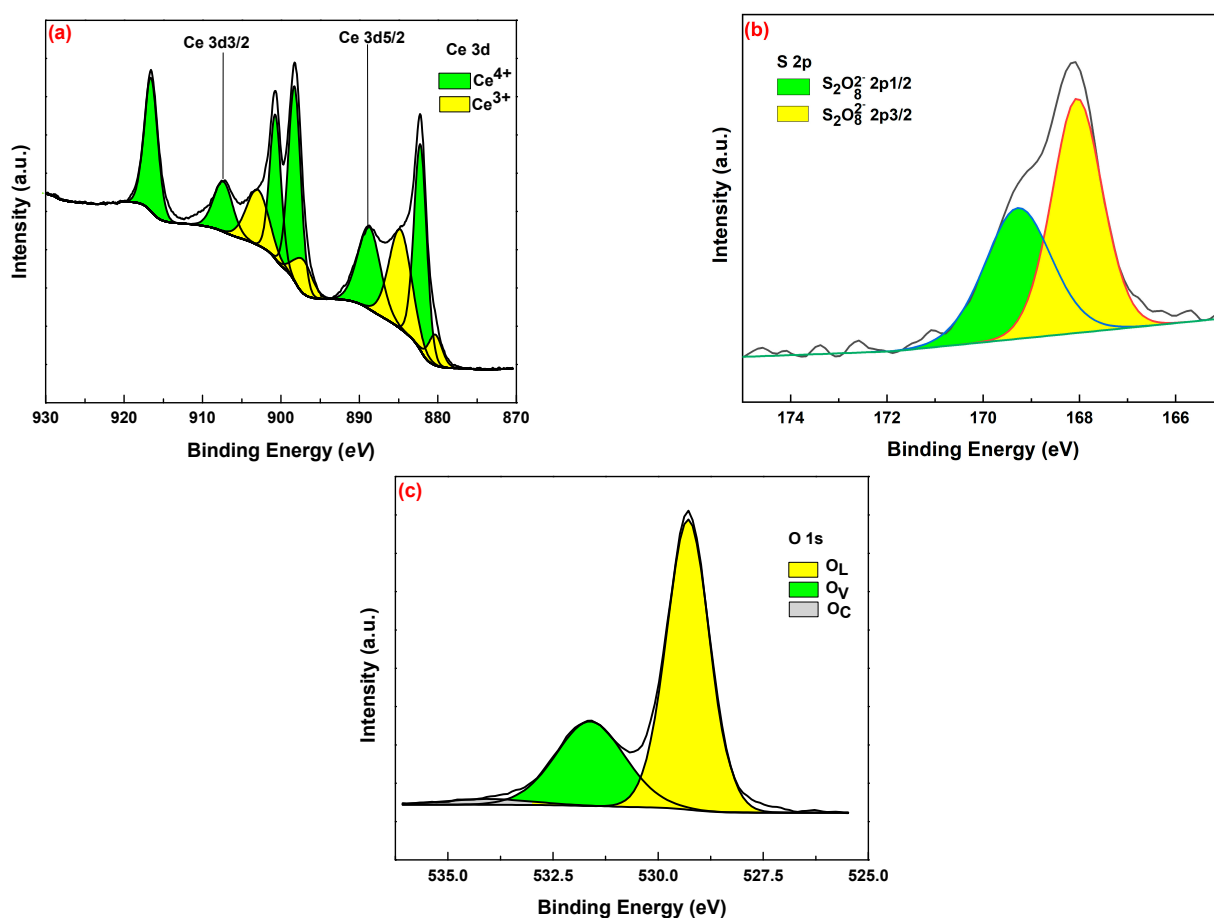
Figure 8. XPS spectrum of representative SC-RF-600: (**a**) Ce 3d spectra, (**b**) S 2p spectra, (**c**) O 1s spectra.

As indicated, Figure 8b shows the XPS spectra of S 2p, compared with the binding energy of S 2p in pristine $(NH_4)_2S_2O_8$ (S 2p3/2 170.8 eV and S 2p1/2 171.2 eV) [39]. The binding energy of S 2p3/2 and S 2p1/2 in all samples decreased; as the density of the electron-cloud around the S atom was increased, correspondingly, the acidity of the catalyst was increased. Among them, the binding energy of S 2p in SC-RF-600 (S 2p3/2 168.1 eV and S 2p1/2 169.3 eV) was the lowest, which showed that RF plasma modification effectively enhanced Lewis acidity.

The O 1s spectra (Figure 8c) are deconvoluted into three different near-Gaussian sub-peaks, where the binding energies are 528.8 eV, 531.1 eV, and 532.2 eV, respectively [19]. The binding energy at 528.8 eV was attributed to the lattice oxygen (O_L) of CeO_2; the binding energy at 532.2 eV represented oxygen vacancy (O_V), indicating that Ce had unsaturated coordination sites to create LA sites, and the binding energy at 531.1 eV represented chemisorbed oxygen (O_C) or OH species [31,40].

Based on XPS measurements, Table 4 summarizes the relative content of different elements on the sample surface (*at%/at%*). With increasing temperature, the amount of O_V and the relative content of Ce^{3+} were increased, and the content of S was decreased (Entrys 1–3), because the temperature increased, the oxygen in the lattice was separated to form O_V, and part of $S_2O_8^{2-}$ decomposed at high temperature. Compared with SC-600 (Entry 3), the content of carbon over SC-RF-600 (Entry 4) was decreased by 19.4% and the content of O_V was increased by 2.59%, indicating that CeO_2 modified by RF plasma effectively reduced carbon contamination over the catalyst surface, increased the content of O_V, and facilitated the formation of surface LA. The relative content of Ce^{3+} was increased by 2.63%, and Ce^{3+} induced O_V generation in the material. The above analysis showed that RF plasma modification effectively increased O_V content and LA sites.

Table 4. Elemental contents of the samples.

| Entry	Sample	Atomic Content (at%)					
		C 1s	Ce 3d	O 1S	S 2p	O_V	$Ce^{3+}/(Ce^{3+} + Ce^{4+})$
1	SC-400	35.47	9.78	49.16	5.58	21.61	26.44
3	SC-500	34.69	10.85	49.32	5.13	24.55	26.84
3	SC-600	31.35	11.83	51.95	4.88	28.52	28.73
4	SC-RF-600	11.95	17.42	58.37	4.64	31.11	31.36

In summary, the results above showed that CeO_2 was modified by RF plasma and then calcined at 600 °C, which led to a higher crystallinity of the catalyst, more oxygen vacancies formed, and a larger specific surface area via XRD and HR-TEM analysis. Combining FT-IR, Py-IR, and BET analysis, it was found that SC-RF-600 formed more O=S=O characteristic functional groups, higher Lewis acid density, and larger specific surface area, which verified the crystal structure and the microstructure of the catalyst. XPS analysis results further proved that RF plasma modified-CeO_2 formed more oxygen vacancies.

2.8. Catalytic Performance

First, the effects of different process parameters on the product yield (mol%) were studied using the single variable method. Figure 9a shows the effect of N_2 pressure (0–2 MPa) on the reaction. First, the TrpOMe (see its HPLC chromatogram in Figure S2) yield reached 43% at 0 MPa, which was caused by partial auto-catalytic esterification, apart from SC-RF-600 catalysis at this reaction condition, and this was confirmed by data in Figure 9c. Then, when the pressure increased from 0 MPa to 1 MPa (at 150 °C and 9 h), the yield reached a high level (85.4%). Appropriately increasing the pressure was conducive to overcoming steric effects [41] and improving the product yield. Therefore, 1 MPa was selected as the appropriate reaction pressure.

Figure 9b shows the effect of temperature (135–195 °C) on the yield of TrpOMe. At 1 MPa and 9 h, the yield of TrpOMe reached 83.7% when the temperature rose to 150 °C, and decreased to 81.6% when the temperature ranged from 150 °C to 195 °C. The decrease in TrpOMe yield during the above period was due to the activity decrease caused by the carbon deposition, which was formed owing to the higher acidity over catalyst surface under the higher temperature [42]. Therefore, 150 °C was selected as the optimal reaction temperature.

At 150 °C and 1 MPa, sampling at intervals between 1–6 h was adopted to collect the product yield catalyzed by the four catalysts, as shown in Figure 9c. It depicted that the esterification equilibrium was reached at around 3–5 h for the four catalysts, with the Trp conversion rate > 99 wt.% during 2–6 h (determined by calculating the dry weight difference of Trp and catalyst mixture before and after the reaction in Figure S3). But the reaction equilibrium with the highest TrpOMe yield was achieved for SC-RF-600 (followed by the catalytic performance of SC-600, SC-500, and SC-400), with the TrpOMe yield reaching 94.5%, apparently shortened the reaction time compared with consuming 20 h catalyzed by H_2SO_4 and dimethyl carbonate and 24 h catalyzed by thionyl chloride, accompanied with environmental polluting [43,44]. Reaction rates were decreasing with the increase in conversion before the equilibriums, then all TrpOMe yields were decreased after 6 h because both Trp and TrpOMe were destroyed over a long time and strong acid environment. Additionally, the blank control group without a catalyst maintained the lowest level in comparison with the others, as Trp was able to undergo a certain degree of auto-catalysis (with the highest yield of 43.2% at 2.5 h) under reaction conditions. Consequently, the solid superacid in our work demonstrated a better ability to catalyze the esterification of Trp.
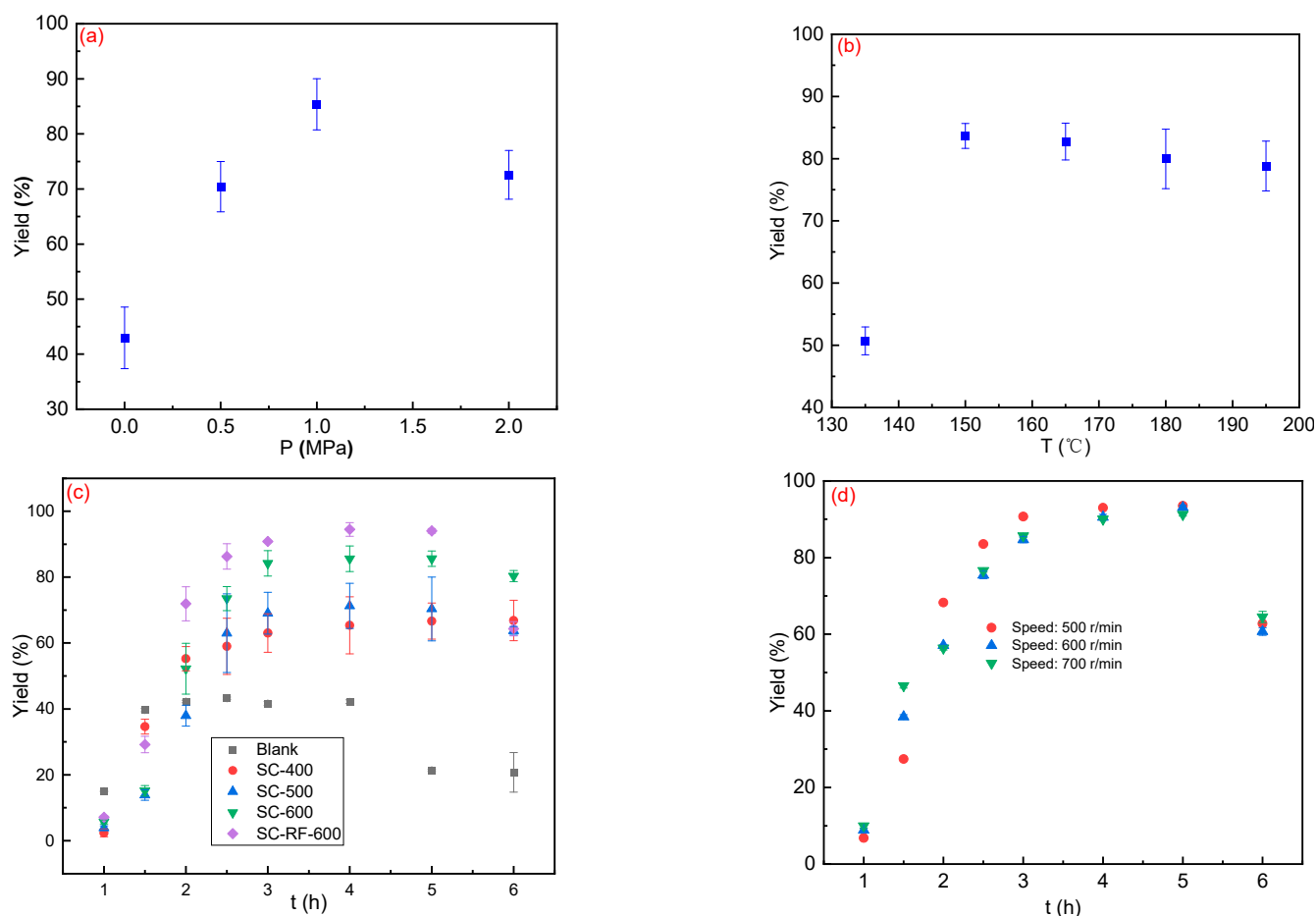
Figure 9. Variation in process parameters: (**a**) Product yield (mol%) over SC-600 vs. N_2 pressure (MPa), reaction conditions: 50 mg catalyst, 0.0025 mol Trp, 0.5 mol methanol, 150 °C, 9 h, 500 rpm; (**b**) product yield (mol%) over SC-600 vs. temperature (°C), reaction conditions: 50 mg catalyst, 0.0025 mol Trp, 0.5 mol methanol, 1 MPa N_2, 9 h, 500 rpm; (**c**) TrpOMe yield (mol%) over the different solid superacid, reaction conditions: 50 mg catalyst, 0.0025 mol Trp, 0.5 mol methanol, 150 °C, 1 MPa N_2, 6 h, 500 rpm; (**d**) the effect of rotating speed on the product yield, reaction conditions: 50 mg catalyst, 0.0025 mol Trp, 0.5 mol methanol, 1 MPa N_2, 6 h.

Lastly, even though the rotating speed (from 500 rpm to 700 rpm) was increased, it did not have a significant influence on the reaction rate in Figure 9d. Therefore, we will focus on reducing catalyst particle size and increasing catalyst pore diameter to eliminate the influence of internal diffusion on the reaction rate in future studies.

From the above results, the catalyst modified by RF plasma effectively improved the esterification reaction rate of Trp and the esterification yield.

In term of the by-product during Trp esterification, such as L-Tryptophan, N-ethoxy carbonyl-, ethyl ester and 3-(1-methoxyvinyl)-1,9-dimethyl-2,3,4,9-tetrahydro-1H-pyrido[3,4-b] indole (Figure S4), which were produced via excessive dehydration of TyrOMe with methanol solvent under a highly acidic environment.

3. Experiments

3.1. Materials

Ce(NO$_3$)$_3$·6H$_2$O (purity > 99.5%), NaOH (purity > 97%), (NH$_4$)$_2$S$_2$O$_8$ (purity > 99%, electrophoretic grade), CH$_3$OH (AR, purity > 99.5%), and 2, 4-Dinitrofluorobenzene (2,4-DNFB, GC, purity > 98.0%) were purchased from Shanghai Macklin Biochemical Co., Ltd., Shanghai, China. 3-Nitrotoluene (3-NT, GC, purity > 99.0%) was purchased from Shanghai Xianding Biotechnology Co., Ltd., Shanghai, China.

3.2. Catalyst Preparation

CeO_2 nanorods were synthesized by the hydrothermal method [45]: firstly, 14.40 g of NaOH was dissolved in 20 mL of deionized water (DIW), 1.30 g of $Ce(NO_3)_3 \cdot 6H_2O$ was dissolved in 40 mL of DIW; and then the two solutions were mixed in a Teflon liner and stirred magnetically (SLR, Wiggens, Straubenhardt, Germany) for 30 min; finally, the Teflon liner was sealed in a stainless steel hydrothermal autoclave (KH-100, Mojina Instrument Manufacturing Co., Ltd., Xi'an, China) and kept at 100 °C for 24 h. The precipitate was collected, washed with DIW until pH = 7, washed twice with anhydrous ethanol successively, and then dried in an oven (DZF-6050AB, Shanghai Shanzhi Instrument Equipment Co., Ltd., Shanghai, China) at 60 °C for 16 h to obtain the final CeO_2. Lastly, CeO_2 was modified with RF plasma generator (self-made, power: 90 W, frequency: 1.86 MHz) in an Ar atmosphere (purity: 99.999%, flow rate: 0.2 L·min^{-1}) for 30 min. As shown in Figure 10, the RF plasma system was equipped with a DC power supply (DQ-2000-400, Nantong Dingqi Electric Co., Ltd., Nantong, China), a signal generator (DG4E211, Puyuan Precision Technology Co., Ltd., Beijing, China), and a vacuum pump (2XZ-2, Shanghai Haoxin Electromechanical Equipment Co., Ltd., Shanghai, China).
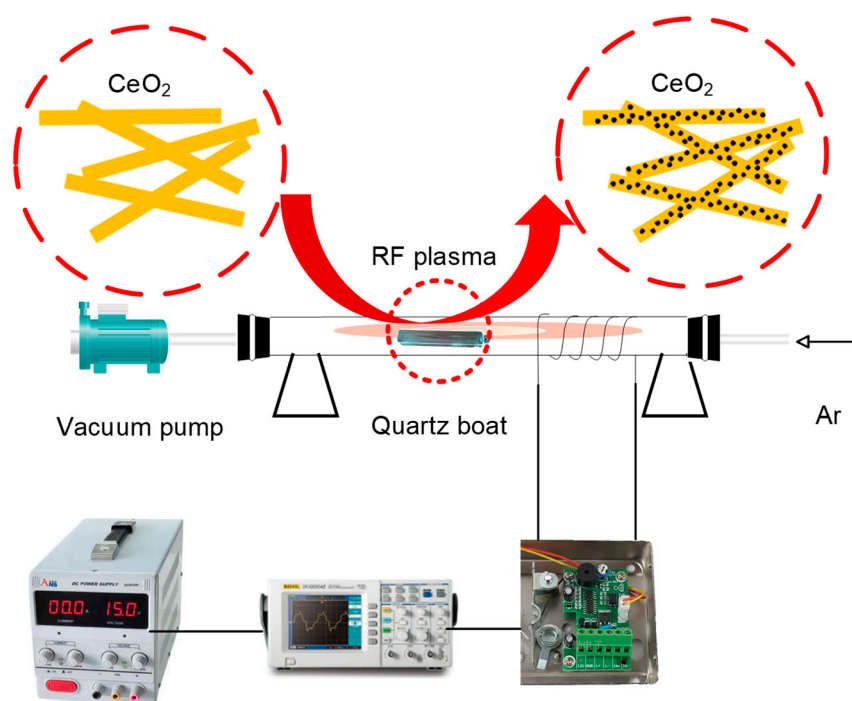
Figure 10. A scheme showing CeO_2 by RF plasma modification.

SC-RF-600 was synthesized as follows: first, 11.41 g of $(NH_4)_2S_2O_8$ was dissolved in 50 mL of DIW to prepare $(NH_4)_2S_2O_8$ solution with 1 mol·L^{-1} and 1.72 g of CeO_2 was introduced and stirred evenly. The mixture was sonicated (800 W, 20 KHz, 30% amplitude, Soncis VXC800, Soncis & Materials, INC., Newtown, CT, USA) for 10 min; then, the catalyst precursor was obtained by stirring for 30 min, standing for 3 h, centrifugation (TG16-WS, Beijing Hongda Hengye Technology Co., Ltd., Beijing, China, 10,000 rpm, 10 min), and vacuum-dried at 110 °C for 3 h. Finally, the catalyst SC-RF-600 was acquired by calcining the precursor at 600 °C for 4 h (Muffle furnace, GWM4-1200L7, Beijing Saiou Huachuang Technology Co., Ltd., Beijing, China). $S_2O_8^{2-}/CeO_2$-400 (SC-400), $S_2O_8^{2-}/CeO_2$-500 (SC-500), $S_2O_8^{2-}/CeO_2$-600 (SC-600) were prepared with CeO_2 as the carrier by the same method.

3.3. Catalyst Characterization

The acid strengths of the catalysts were examined using Hammett indicators. Typically, the catalyst was heated under vacuum at 200 °C for 2 h. The titration was carried out by dispersing 25 mg catalyst, 0.25 mL dry benzene, and 50 mg Hammett indicator in a tube, heating in an oil bath (60 °C) for 30 min, and then observing the color change of the catalysts surface.

X-ray diffraction (XRD, X'Pert-ProMPD, PANalytical Company, Almelo, Netherlands) analysis was performed with Cu Kα radiation (λ = 0.154 nm) at 40 mA and 40 kV, to analyze solid superacid crystallinity in the *2θ* range of 5–90° (RT).

Structural information was obtained using high resolution transmission electron microscopy (HR-TEM), with a high angle annular dark-field scanning transmission electron microscope (JEM-2100, JEOL Ltd., Tokyo, Japan).

N_2 adsorption–desorption experiments were performed at −196 °C (Tristar II 3020 3.02, Micromeritics Instrument Co., Ltd., Norcross, GA, USA). The specific surface area of each catalyst was calculated using the Brunauer–Emmett–Teller (BET) method for the isotherms, while pore size distribution was calculated using the Barrett–Joyner–Halenda (BJH) model of the adsorption branch of isotherms.

X-ray photoelectron spectroscopy (XPS, ESCALAB 250Xi, Thermo Fisher Scientific Inc., Waltham, MA, USA) of samples was conducted using X-ray radiation generated by Al Kα (1486.6 eV) and analyzed in a vacuum chamber. Binding energy (BE) data were analyzed using Advantage software (version 5.984, Thermo Fisher Scientific Inc.) following ISO 15,472 [46], and calibrated with a carbon reference (C1s = 284.8 eV) of aliphatic hydrocarbon.

The catalysts were characterized by Fourier transform infrared spectroscopy (FT-IR; Nicolet 6700, Nicolet Instrument Company, Orlando, FL, USA) using the KBr pellet method (2 cm^{-1} resolution from 400 to 4000 cm^{-1}) in transmission mode, with spectra normalized to the maximal value. The acid density (μmol·g^{-1}) of samples was examined using a pyridine absorbed infrared spectrometer (Py-IR). Each sample was vacuum-activated (at 200 °C) for 0.5 h, and then the sample was cooled to 50 °C to record the background spectrum. Firstly, the catalyst was exposed to pyridine vapor for 15 min. Afterward, the Py-IR spectrum was acquired after pyridine desorption by evacuation for 0.5 h (at 150 °C and 300 °C). Finally, the Py-IR spectrum was recorded by subtracting the background spectrum (RT).

3.4. Catalytic Esterification

First, 50 mg catalyst was mixed with 0.0025 mol Trp, and the blend added to 0.5 mol methanol in an autoclave (50 mL, MSC50-P5-T3, Hefei Safety Instrument Co., Ltd., Hefei, China) equipped with a sampling reflux device. Then, the autoclave was purged by N_2 (purity $\geq$ 99.9%) three times to eliminate residual air. The experiment was conducted at a specific temperature and N_2 pressure (RT) with a rotating speed of 500 rpm, and adopted a time-sampling method to calculate TrpOMe yield. Subsequently, the reaction was terminated using an ice-water bath with the post-reaction mixture and the catalyst separated through a nylon Millipore filter (0.22 μm, Tianjin Jinteng Instrument Factory, Tianjin, China). A comparison of physical properties (viscosity, density, and water content) of obtained TrpOMe and commercial TrpOMe is listed in Table S2. It was discovered that these parameters for the two chemicals were quite close, indicating the obtained product had a high purity.

A qualitative analysis of the filtrate was conducted using GC-MS (Thermo Fisher Scientific Inc., Waltham, MA, USA), which consisted of a Trace 1310 gas chromatograph coupled with a TSQ 9000 triple quadrupole mass spectrometer. The TrpOMe yield was quantitated by HPLC (Infinity II), equipped with a C18 column (Agilent Eclipse Plus, 4.6 × 250 mm, 5 μm) and UV-DAD detection (G7115, Agilent Technology, Santa Clara, CA, USA). Chromatographic conditions: column temperature 50 °C, mobile phase containing CH_3OH and 5 mM CH_3COONH_4 (2:3, *V*/*V*), and detection wavelength 280 nm. The

concentration of TrpOMe (mg·mL^{-1}) was quantified by external standard calibration e ($R^2 > 0.999$). The yield calculation is shown in Equation (2):

$$Y(\text{wt.\%}) = \frac{c \cdot V}{M \cdot n \cdot 1000} \times 100 \tag{2}$$

where, Y was the yield of TrpOMe (wt.%); C was the concentration of TrpOMe (mg·mL^{-1}); V was the volume of reaction mixture (mL); M was the molecular mass of TrpOMe; n was the amount of Trp (mol) added.

4. Conclusions

Here, the SC-RF-600 solid superacid was successfully prepared using a combination of hydrothermal methods and RF plasma modification. It was found that the calcination temperature mainly affected the crystallinity and acid density of the solid superacid. With the increase in temperature, the crystal size of the catalyst gradually became larger and the crystal shape tended to be complete, which was more conducive to the formation of a solid superacid structure. More importantly, RF plasma improved the dispersion, prevented particle agglomeration/grain growth, increased the specific surface area, and increased oxygen vacancy concentration of the catalyst effectively due to its special etching effects. Finally, SC-RF-600 modified by RF plasma had a better catalytic performance on the esterification of Trp than SC-600 prepared by a conventional method, and the yield of TrpOMe reached 94.5% at 150 °C and 1 MPa for 2 h over SC-RF-600. This work has expanded the application potential of plasma technology in the field of solid superacid catalyst preparation/modification, and this type of catalyst can promote the esterification reaction of aromatic amino acids with amphoteric dissociation effects.

References

1. Chen, H.Z.; Zhang, Y.; Xue, F.; Sun, Z.L. Research progress of SO_4^{2-}/M_xO_y solid superacid catalysts. *Chem. Ind. Eng. Prog.* **2018**, *37*, 1759–1809.
2. Hino, M.; Kobayashi, S.; Arata, K. Solid catalyst treated with anion. 2. Reactions of butane and isobutane catalyzed by zirconium oxide treated with sulfate ion. Solid superacid catalyst. *J. Am. Chem. Soc.* **1979**, *101*, 6439–6441. [CrossRef]
3. Wang, H.G.; Shi, G.L.; Yu, F.; Li, R.F. Mild synthesis of biofuel over a microcrystalline $S_2O_8^{2-}$/ZrO_2 catalyst. *Fuel Process. Technol.* **2016**, *145*, 9–13. [CrossRef]
4. Xia, Y.D.; Hua, W.M.; Gao, Z. *n*-Butane isomerization on solid superacids of ZrO_2 modified by persulfate. *J. Chem.* **1999**, *57*, 1325–1331.
5. Li, P.; Gu, Y.; Yu, Z.; Gao, P.; An, Y.; Li, J. TiO_2-SnO_2/SO_4^{2-} mesoporous solid superacid decorated nickel-based material as efficient electrocatalysts for methanol oxidation reaction. *Electrochim. Acta* **2019**, *297*, 864–871. [CrossRef]

6. Dzhikiya, O.V.; Smolikov, M.D.; Zatolokina, E.V.; Kazantsev, K.V.; Belyi, A.S. Isomerization of *n*-hexane on $Pd/SO_4^{2-}/ZrO_2/Al_2O_3$ and mechanical mixtures Pd/Al_2O_3 (Pd/SiO_2) + $SO_4^{2-}/ZrO_2/Al_2O_3$. *Procedia Eng.* **2016**, *152*, 116–121. [CrossRef]

7. Lin, F.; Shao, B.; Li, Z.; Zhang, J.Y.; Wang, H.; Zhang, S.H.; Haruta, M.; Huang, J.H. Visible light photocatalysis over solid acid: Enhanced by gold plasmonic effect. *Appl. Catal. B Environ.* **2017**, *218*, 480–487. [CrossRef]

8. Zhang, S.; Su, L.; Liu, L.; Fang, G.Z. Degradation on hydrogenolysis of soda lignin using $CuO/SO_4^{2-}/ZrO_2$ as catalyst. *Ind. Crops Prod.* **2015**, *77*, 451–457. [CrossRef]

9. Song, Z.; Zhang, Q.; Liu, X.; Fan, J.; Huang, Z. Introduction manner of sulfate acid for improving the performance of SO_4^{2-}/CeO_2 on selective catalytic reduction of NO by NH_3. *J. Rare Earths* **2016**, *34*, 667–674. [CrossRef]

10. Li, S.X.; Xu, Y.R.; Wang, S. Preparation of solid superacid SO_4^{2-}/TiO_2-HZSM-5 catalyst and its catalytic performance in esterification. *Chem. Ind. Eng. Prog.* **2015**, *34*, 745–750.

11. Li, J.; Ma, C.; Zhu, S.; Yu, F.; Dai, B.; Yang, D. A Review of recent advances of dielectric barrier discharge plasma in catalysis. *Nanomaterials* **2019**, *9*, 1428. [CrossRef]

12. Duan, S.; Liu, X.; Wang, Y.; Meng, Y.; Alsaedi, A.; Hayat, T.; Li, J. Plasma surface modification of materials and their entrapment of water contaminant: A review. *Plasma Process. Polym.* **2017**, *14*, 1600218. [CrossRef]

13. Li, H.P.; Yu, D.R.; Sun, W.T.; Liu, D.X.; Li, J.; Han, X.W.; Li, Z.Y.; Sun, B.; Wu, Y. State-of-the-art of atmospheric discharge plasmas. *High Volt. Eng.* **2016**, *42*, 3697–3727.

14. Xia, S.Y.; Mi, J.F.; Du, S.N. Research progress of non-thermal plasma treatment of volatile organic compounds. *Appl. Chem.* **2021**, *50*, 1130–1135.

15. Su, F.-M.; Zhang, D.; Liang, F. Progress in preparation and modification of nano-catalytic materials by low-temperature plasma. *Chin. J. Appl. Chem.* **2019**, *36*, 882–891.

16. Wang, B.; Xiong, Y.; Han, Y.; Hong, J.; Zhang, Y.; Li, J.; Jing, F.; Chu, W. Preparation of stable and highly active Ni/CeO_2 catalysts by glow discharge plasma technique for glycerol steam reforming. *Appl. Catal. B Environ.* **2019**, *249*, 257–265. [CrossRef]

17. Li, Y.; Jang, B.W.L. Selective hydrogenation of acetylene over Pd/Al_2O_3 catalysts: Effect of non-thermal RF plasma preparation methodologies. *Top. Catal.* **2017**, *60*, 997–1008. [CrossRef]

18. Xu, L.; Jiang, Q.; Xiao, Z.; Li, X.; Huo, J.; Wang, S.; Dai, L. Plasma-engraved Co_3O_4 nanosheets with oxygen vacancies and high surface area for the oxygen evolution reaction. *Angew. Chem. Int. Ed. Engl.* **2016**, *55*, 5277–5281. [CrossRef] [PubMed]

19. Huang, H.; Dai, Q.; Wang, X. Morphology effect of Ru/CeO_2 catalysts for the catalytic combustion of chlorobenzene. *Appl. Catal. B Environ.* **2014**, *158–159*, 96–105. [CrossRef]

20. Griehl, C.; Weigt, J.; Jeschkeit, H. Use of tryptophan peptides for an HPLC racemization test with fluorescence detection. *J. High Resolut. Chromatogr.* **1994**, *17*, 700–704. [CrossRef]

21. Xiong, J.; Zhu, H.F.; Zhao, Y.J.; Lan, Y.J.; Jiang, J.W.; Yang, J.J.; Zhang, S.F. Synthesis and antitumor activity of amino acid ester derivatives containing 5-fluorouracil. *Molecules* **2009**, *14*, 3142–3152. [CrossRef]

22. Vinod, V.T.P.; Sashidhar, R.B.; Sarma, V.U.M.; Raju, S.S. Comparative amino acid and fatty acid compositions of edible gums kondagogu (*Cochlospermum gossypium*) and karaya (*Sterculia urens*). *Food Chem.* **2010**, *123*, 57–62. [CrossRef]

23. Zhu, C.; Wang, K.; Luo, J.; Tian, B.; Sun, J.; Liu, X.; Zhu, W.; Zou, Z. Solid superacid SO_4^{2-}-$S_2O_8^{2-}/SnO_2$-Nd_2O_3 catalyzed esterification of *α*-aromatic amino acids. *Mol. Catal.* **2023**, *535*, 112833. [CrossRef]

24. Paul, M.A.; Long, F.A. H_0 and related indicator acidity function. *Chem. Rev.* **1957**, *57*, 1–45. [CrossRef]

25. Zhang, Y.H.; Xu, Y.; Chen, C.G.; Ou, Z.W. Studies on the formation mechanism of SO_4^{2-}/ZrO_2 solid superacid. *J. Chongqing Univ. (Nat. Sci. Ed.)* **1999**, *20*, 77–81.

26. Monshi, A.; Foroughi, M.R.; Monshi, M.R. Modified Scherrer equation to estimate more accurately nano-crystallite size using XRD. *World J. Nano Sci. Eng.* **2012**, *2*, 154–160. [CrossRef]

27. Bingfu, L.; Ken-ichi, M.; Takashi, H.; Hanzawa, H. Synthesis and photoluminescence properties of $CaAlSiN_3$: Eu^{2+} nanocrystals. *Chem. Lett.* **2010**, *39*, 104–105.

28. Huang, Z.; Deng, J.; Wang, H.; Zhang, Y.; Duan, J.; Tang, Z.; Cao, Z.; Qi, J.; He, D.; Lu, T. Fast low-temperature densification of translucent bulk nanograin $Gd_2Zr_2O_7$ ceramics with average grain size below 10 nm. *J. Alloys Compd.* **2020**, *830*, 154617. [CrossRef]

29. Wang, W.W.; Yu, W.Z.; Du, P.P.; Xu, H.; Jin, Z.; Si, R.; Ma, C.; Shi, S.; Jia, C.J.; Yan, C.H. Crystal plane effect of ceria on supported copper oxide cluster catalyst for CO oxidation: Importance of metal–support interaction. *ACS Catal.* **2017**, *7*, 1313–1329. [CrossRef]

30. Wu, Z.; Li, M.; Overbury, S.H. On the structure dependence of CO oxidation over CeO_2 nanocrystals with well-defined surface planes. *J. Catal.* **2012**, *285*, 61–73. [CrossRef]

31. Song, H.; Cui, H.; Song, H.; Li, F. The effect of Zn–Fe modified $S_2O_8^{2-}/ZrO_2$-Al_2O_3 catalyst for *n*-pentane hydroisomerization. *Res. Chem. Intermed.* **2015**, *42*, 3029–3038. [CrossRef]

32. Zhao, Q.; Meng, S.; Wang, J.; Li, Z.; Liu, J.; Guo, Y. Preparation of solid superacid $S_2O_8^{2-}/TiO_2$–exfoliated graphite (EG) and its catalytic performance. *Ceram. Int.* **2014**, *40*, 16183–16187. [CrossRef]

33. Gu, Y. Honeycomb-like mesoporous NiO-SnO_2/SO_4^{2-} solid superacid for the efficient reaction of methanol oxidation. *Int. J. Electrochem. Sci.* **2020**, *15*, 2481–2498. [CrossRef]

34. Song, H.; Zhao, L.; Wang, N.; Li, F. Isomerization of *n*-pentane over La-Ni-$S_2O_8^{2-}/ZrO_2$-Al_2O_3 solid superacid catalysts: Deactivation and regeneration. *Appl. Catal. A Gen.* **2016**, *526*, 37–44. [CrossRef]

35. Ma, H.-Q. Preparation and catalytic properties study of solid superacid catalyst $S_2O_8^{2-}$/ZrO_2-Al_2O_3: Modified by Lanthanum. *Mater. Guide B* **2014**, *28*, 48–64.
36. Yin, H.L.; Tan, Z.Y.; Liao, Y.-T.; Feng, Y.J. Application of SO_4^{2-}/TiO_2 solid superacid in decontaminating radioactive pollutants. *J. Environ. Radioact.* **2006**, *87*, 227–235. [CrossRef] [PubMed]
37. Zhang, K.Y.; Zhang, P.W.; Yang, G. Study on Pt-SO_4^{2-}-ZrO_2-Al_2O_3 solid superacid catalyst. *Pet. Process. Petrochem.* **2020**, *51*, 33–40.
38. Mai, H.X.; Sun, L.D.; Zhang, Y.W.; Si, R.; Feng, W.; Zhang, H.P.; Liu, H.C.; Yan, C.H. Shape-selective synthesis and oxygen storage behavior of Ceria nanopolyhedra, nanorods. *Am. Chem. Soc.* **2005**, *109*, 24380–24385. [CrossRef]
39. Velmurugan, R.; Krishnakumar, B.; Swaminathan, M. Synthesis of Pd co-doped nano-TiO_2-SO_4^{2-} and its synergetic effect on the solar photodegradation of Reactive Red 120 dye. *Mater. Sci. Semicond. Process.* **2014**, *25*, 163–172. [CrossRef]
40. Liu, B.; Li, C.; Zhang, G.; Yao, X.; Chuang, S.S.C.; Li, Z. Oxygen vacancy promoting dimethyl carbonate synthesis from CO_2 and methanol over Zr-doped CeO_2 nanorods. *ACS Catal.* **2018**, *8*, 10446–10456. [CrossRef]
41. Degueil-Castaing, M.; Rahm, A. Reduction of ketones by tributyltin hydride: The effect of high pressure on steric hindrance and rearrangement processes. *J. Org. Chem.* **1986**, *51*, 1672–1676. [CrossRef]
42. Eleeza, J.; Boahene, P.; Vedachalam, S.; Adjaye, J. Influence of catalyst acidity on fine particle deposition during hydrotreating of bitumen-derived heavy gas oil. *Energy Fuels* **2021**, *35*, 16735–16749. [CrossRef]
43. Perosa, A. Greeneer Syntheses & Solvents for Fine and Pharmaceutical Chemicals. Ph.D. Thesis, Università Ca' Foscari Venezia, Venezia, Italy, 2012.
44. Justino, A.; Carvalho AC, S.; de Vasconcelos, L.G.; Gai, B.M.; Stein, A.L.; Siqueira, A.B. Tryptophan methyl ester: A proposal of the thermal decomposition mechanism. *J. Therm. Anal. Calorim.* **2022**, *147*, 7741–7748. [CrossRef]
45. Hu, X.C.; Fu, X.P.; Wang, W.W.; Wang, X.; Wu, K.; Si, R.; Ma, C.; Jia, C.J.; Yan, C.H. Ceria-supported ruthenium clusters transforming from isolated single atoms for hydrogen production via decomposition of ammonia. *Appl. Catal. B Environ.* **2020**, *268*, 118424. [CrossRef]
46. Zhang, S.; Chen, C.Y.; Jang, B.W.L.; Zhu, A.M. Radio-frequency H_2 plasma treatment of AuPd/TiO_2 catalyst for selective hydrogenation of acetylene in excess ethylene. *Catal. Today* **2015**, *256*, 161–169. [CrossRef]